PAPER • OPEN ACCESS

Experimental and simulation studies on damage mechanisms of tungsten and molybdenum under compressed plasma flow irradiation

OPEN ACCESS
IOP Publishing | International Atomic Energy Agency
Nuclear Fusion
Nucl. Fusion **63** (2023) 076010 (14pp)
https://doi.org/10.1088/1741-4326/acd016

Experimental and simulation studies on damage mechanisms of tungsten and molybdenum under compressed plasma flow irradiation

Lisong Zhang[1], Xiaonan Zhang[1,2], Na Li[1], Peng Zhang[1], Xianxiu Mei[1,*], Younian Wang[1] and Vladimir V Uglov[3]

[1] Key Laboratory of Materials Modification by Laser, Ion and Electron Beams, Ministry of Education, Dalian University of Technology, Dalian 116024, China
[2] School of Science, Dalian Jiaotong University, Dalian 116028, China
[3] Belarusian State University, Minsk 220030, Belarus

E-mail: xxmei@dlut.edu.cn

Received 13 January 2023, revised 1 April 2023
Accepted for publication 25 April 2023
Published 25 May 2023

Abstract

The failure mechanism of plasma-facing components (PFCs) under extreme plasma conditions relevant for fusion reactors were investigated. Here, edge-localized mode (ELM)-like transient thermal shock irradiation experiments were performed on tungsten and molybdenum using compressed plasma flow, and combined with thermal–mechanical analysis by means of finite element simulations to discuss the grain structure evolution, cracking behavior and variations of hardness. When ELM-like thermal shock irradiation was sufficient to melt tungsten and molybdenum, a submicron-sized cellular sub-grain structure was created on their surface due to the high temperature gradient of the molten layer under the effect of Bénard–Marangoni instability. Rapid directional solidification from the bottom of the molten layer to the surface induced the formation of columnar grains dominated by the <200> orientation. While the formation of cellular sub-grains increased hardness, the thermal effect of irradiation and the formation of columnar grains led to softening. The high thermal stress induced by the ELM-like thermal shock produced macro-cracks and micro-cracks on the surface of tungsten and only micro-cracks on the surface of molybdenum. Macro-cracks were generated due to the intrinsic brittleness of tungsten. As a result of stress evolution, longitudinal macro-cracks extending perpendicular to the surface experienced transverse transformation within the material. Micro-cracks formed due to the embrittlement of the re-solidification zone, and their width increased with the melting depth. These results help us to understand failure mechanisms in PFCs under extreme operating conditions and are valuable for developing future fusion reactors.

* Author to whom any correspondence should be addressed.

Keywords: tungsten, molybdenum, ELM-like thermal shock, compressed plasma flow, finite element method

(Some figures may appear in colour only in the online journal)

1. Introduction

High-power edge-localized mode (ELM) bombardment is one of the greatest lifetime and performance challenges for plasma-facing materials (PFMs) in future fusion reactors, whose transient power densities can exceed 1 GW m^{-2} [1–3]. Tungsten is intended to be used as a first-wall PFM of ITER, for example as a divertor, due to its high melting point, high thermal conductivity and low sputtering yield [3–5]. Molybdenum has the advantage of a high melting point as well as high reflectivity retention after sputtering, and is regarded as a candidate for the first mirror PFM [6–8]. It is important to study the irradiation damage mechanisms of tungsten and molybdenum under ELM-like transient thermal shock.

Materials are subjected to strong heat and high temperature gradients during the process of ELM thermal shock irradiation. Strong thermal effects can lead to material recrystallization, melting and even ablation, while high temperature gradients can bring about high thermal stress and induce cracking, either of which can affect the mechanical properties of the PFM and thus shorten the service life [3]. When ELM-like thermal shock irradiation is sufficient to melt the material, the re-solidified layer tends to form a columnar grain structure [9–11]. A submicron-sized cellular sub-grain structure is also frequently seen on the surface of materials after ELM-like thermal shock irradiation [10, 12–20]. However, researchers are not unanimous in their interpretation of the formation of the cellular sub-grain structure. Makhlay *et al* [14] suggested that this formation process might be related to the high-speed quenching of the surface layer. Li *et al* [20] argued that this was the result of the accumulation of dislocations induced by high plastic deformation of the surface. Shymanski *et al* [12] suggested that the separation of light impurities (like carbon or oxygen) in the material before crystallization could lead to the disturbances of free surface and consequent creation of such a structure. Although Qu *et al* [13] were unable to determine the cause of the formation of the cellular sub-grain structure, they suggested that its size might be related to the viscosity of the molten material. After irradiation, macro-cracks and micro-cracks appear on the tungsten surface [19, 21]. Macro-cracks occur due to the intrinsic brittleness of the material, while micro-cracks are related to the melting and re-solidification process [13]. Besides the ductile-to-brittle transition temperature (DBTT) of the material [22], the heat flux factor of the thermal shock irradiation [23], the base temperature of the material during irradiation [24, 25] and the processing history of the material [26] are the key factors affecting macro-crack generation. Moreover, longitudinal macro-cracks extending perpendicular to the surface may undergo transverse transformation within the material [27, 28].

A pulsed plasma [13, 21, 29], high-power electron beam [26, 30] and strong laser [31, 32] are commonly used for the experimental study of ELM-like thermal shocks due to the limitation of the amount of experimental equipment available for large-scale fusion reactions. Previous experiments showed that the materials exhibited similar damage behavior and damage thresholds for different thermal loading techniques [17, 33, 34], all of which have good reliability in testing the transient thermal shock resistance of materials. In terms of simulation, the finite element method, based on the heat conduction equation and the theory of elasto-plastic mechanics, is capable of reconstructing the distributions of temperature and thermal stress quickly and accurately, and is often used in the thermal–mechanical analysis of materials in the process of thermal shock irradiation [23, 35, 36]. The combination of ELM-like thermal shock irradiation experiments and finite element method simulation is very helpful for understanding the mechanism of generation and evolution of irradiation damage.

In this study, pure tungsten and pure molybdenum were irradiated using a compressed plasma flow (CPF) with different energy densities, and the evolutions of temperature and thermal stress/strain of the materials in time and space during irradiation were simulated by the finite element method. Combining the results of experiments and simulation, the grain structure evolution, cracking behavior and hardness changes of tungsten and molybdenum under ELM-like transient thermal shock are discussed.

2. Methods of experiments and simulation

Commercial rolled plates of pure tungsten and pure molybdenum (purity >99.99%) from Advanced Technology & Materials Co., Ltd (AT&M) with a size of 10 mm × 10 mm × 2 mm were used as experimental samples. Table 1 shows the physical properties of tungsten and molybdenum at room temperature (RT) (density ρ, specific heat capacity C, thermal conductivity λ, Young's modulus E, Poisson's ratio υ, thermal expansion coefficient α and yield strength σ_s) as well as their latent heats of fusion (L), melting point (T_m), recrystallization temperature (T_r) and the DBTT, which were obtained from the Material Properties Database (MPDB) software and [37, 38]. Prior to irradiation, tungsten and molybdenum were polished to a mirror finish using silicon carbide paper and diamond paste.

All tungsten and molybdenum samples were treated by compressed nitrogen plasma flow at RT. All irradiation experiments were performed with three pulses, and the pulse duration and interval were approximately 100 μs and 20 s, respectively. The experiments were performed in a 'residual gas' mode in which a pre-evacuated vacuum chamber (with the main material being stainless steel) was filled with the working gas (nitrogen) up to a pressure of about 400 Pa. A CPF of 6–10 cm in length with a diameter of 1 cm in the maximum

Table 1. Physical properties of tungsten and molybdenum at room temperature and their L, T_m, T_r and DBTT.

Material	ρ (g cm^{-3})	C (J (kg K)$^{-1}$)	λ (W (m K)$^{-1}$)	E (GPa)	υ	α (K^{-1})	σ_s (MPa)	L (J g^{-1})	T_m (K)	T_r (K)	DBTT (K)
W	19.25	132	173	411	0.28	4.5×10^{-6}	1305	284.3	3695	1478	673
Mo	10.28	251	138	329	0.31	4.8×10^{-6}	546	390.4	2896	1158	413

compression zone was formed in the output of the discharge device. The range of the plasma velocity in the CPF was (4–7) $\times$ 10^6 cm s^{-1}, the concentration of the charged particles in the compression zone was (5–10) $\times$ 10^{17} cm^{-3} and the plasma temperature was 1–3 eV [12, 39]. The samples were placed behind the compression region and attached to the holder by a special conductive adhesive. The energy density (ε) can be changed by altering the distance between the electrode and the sample surface. CPF irradiation experiments were performed at distances of about 16, 12 and 8 cm, respectively. Based on experimental results and prior experience [12, 40], energy densities of the above irradiation were estimated to be about 20, 50 and 80 J cm^{-2}, and the corresponding power densities were about 2, 5 and 8 GW m^{-2}.

The evolution of temperature, stress and strain with time and space in tungsten and molybdenum during CPF irradiation was simulated by the finite element method using Abaqus software. A three-dimensional deformable finite element model was established based on the actual size of sample, as shown in figure A1(a) in the appendix. The analysis type was set to temperature–displacement coupling (transient). For the heat load, since the nitrogen plasma with an energy of only 1–3 eV was injected at a depth of less than 1 nm, i.e. concentrated on the surface of the material, it was assumed that the distribution of heat flow in space was uniformly deposited on the two-dimensional surface. The distribution of heat flow with time was obtained by normalizing the typical current–time curve of CPF irradiation [39], as shown in figure A1(b). Since the heat flow was uniformly distributed on the surface, the heat transfer in x and y directions could be neglected and more attention was paid to the thermal–mechanical analysis in the depth (z) direction. Based on this, the mesh was divided into 21 $\times$ 21 $\times$ 200, sparse in the x and y directions and dense in the z direction. The initial condition used in the calculation was $T_0 = 298$ K (RT). Since the irradiation was performed in a vacuum chamber, the boundary condition for the surface and four sides was set to adiabatic and the boundary condition for the bottom of the sample was set to thermal convection at RT to simulate the heat dissipation from the actual sample to the holder. The temperature-dependent thermal parameters ($\rho(T)$, $C(T)$, $\lambda(T)$) and mechanical parameters ($E(T)$, $\upsilon(T)$, $\alpha(T)$, $\sigma_s(T)$) of tungsten and molybdenum as input in the finite element model were taken from the MPDB software, as shown in figures A1(c)–(e).

The SE-II mode of a scanning electron microscope (SEM; Zeiss SUPRA 55) was used to observe the surface and cross-sectional morphology. The method of making cross-sectional samples was as follows: firstly, the surfaces of two samples were glued together, then a rough cross-section was cut out using a low-speed saw and finally a smooth cross-section was generated by polishing. The electron backscattering diffraction (EBSD) mode of the SEM was used to identify the grain maps. The phase structure before and after irradiation was studied by the $\theta-2\theta$ coupled scan mode of x-ray diffraction (XRD; D8 Discover) with Cu Kα radiation. The hardness variations of the surface were measured by a micro-nano-indenter (FISCHERSOPE HM2000) with an indentation depth of 2 μm and a loading time of 30 s.

3. Experimental results

Figure 1 shows the surface SEM images of tungsten and molybdenum before and after CPF irradiation. For tungsten, no significant damage was observed on the surface after irradiation at an energy density of 20 J cm^{-2}. Macro-cracks were produced on the surface of the tungsten irradiated at 50 J cm^{-2}. When the energy density increased to 80 J cm^{-2}, melting waves and a cellular sub-grain structure appeared on the surface, and micro-cracks were generated in addition to macro-cracks. For molybdenum, the effect of irradiation at an energy density of 20 J cm^{-2} on the surface morphology was not significant. Melting waves, micro-cracks and a cellular sub-grain structure were produced on the surface at energy densities of 50 and 80 J cm^{-2}. No macro-cracks were observed on the molybdenum surface for any of the irradiation parameters. The measurements of crack width and cellular sub-grain size on tungsten and molybdenum surfaces after CPF irradiation are summarized in table 2. For the same material, the crack width and cellular sub-grain size increased with increasing energy density; for the same energy density, the micro-crack width of tungsten was smaller than that of molybdenum, but their cellular sub-grain size was similar.

In order to further investigate crack evolution, the crack cross-sectional morphologies of tungsten and molybdenum were observed after irradiation at energy densities of 50 and 80 J cm^{-2}, as shown in figure 2. For tungsten, two types of macro-cracks including perpendicular to the surface direction (longitudinal) and parallel to the surface direction (transverse) were observed after irradiation at energy densities of 50 and 80 J cm^{-2}. Longitudinal macro-cracks with a depth of about 100–120 μm extended from the surface to the interior, and the majority of transverse macro-cracks were concentrated in the depth range of about 100–150 μm. Interestingly, all longitudinal and transverse cracks connected to each other and the connection points were usually located at the end of the longitudinal cracks, which implied that the transverse cracks extended from the longitudinal cracks. The micro-crack depth of tungsten was about 4 μm when the energy density was 80 J cm^{-2}.

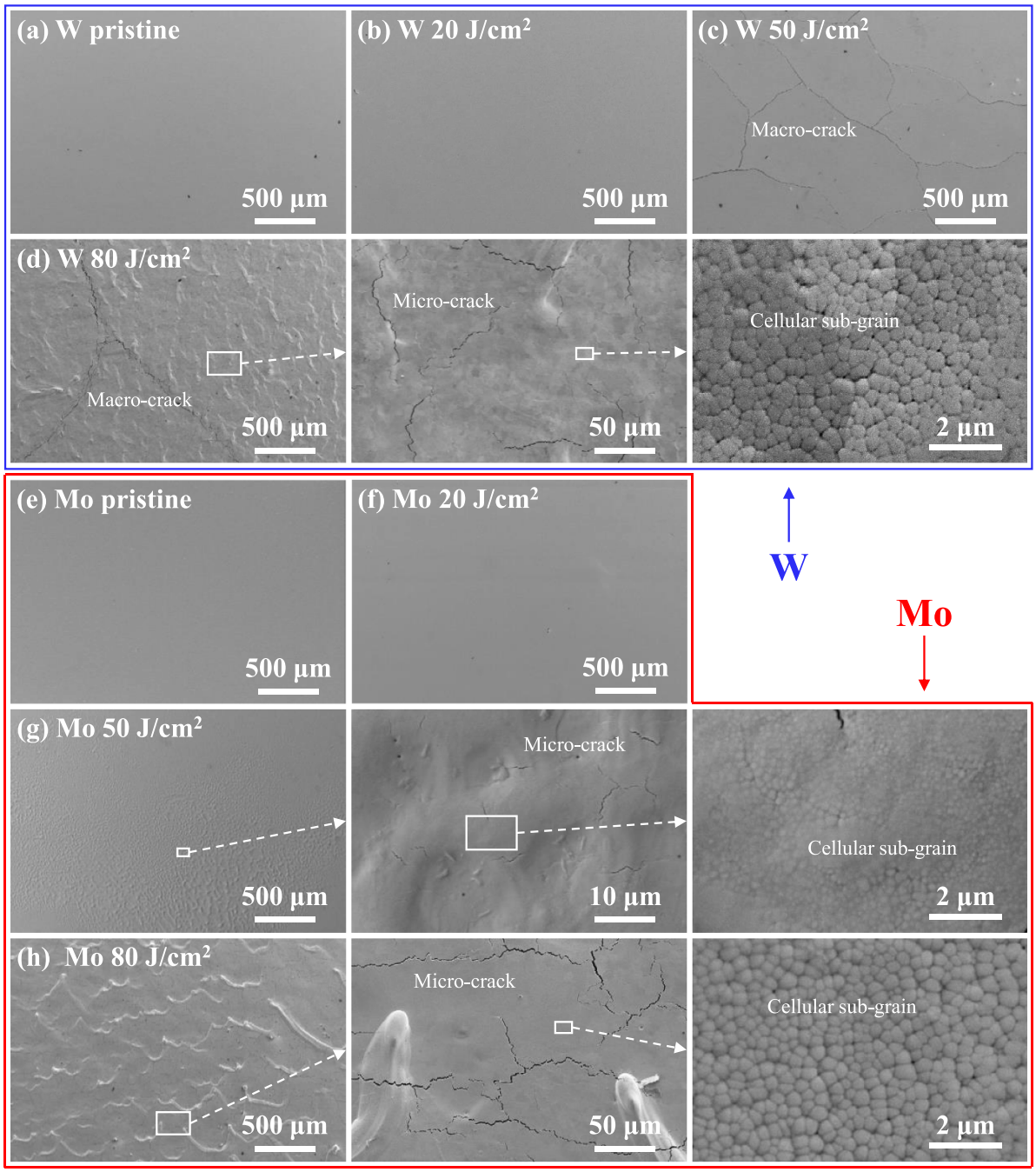

Figure 1. The surface SEM images of tungsten and molybdenum before and after CPF irradiation: (*a*) W pristine, (*b*) W 20 J cm^{-2}, (*c*) W 50 J cm^{-2}, (*d*) W 80 J cm^{-2}, (*e*) Mo pristine, (*f*) Mo 20 J cm^{-2}, (*g*) Mo 50 J cm^{-2}, (*h*) Mo 80 J cm^{-2}.

Table 2. Crack width and cellular sub-grain size.

Material	ε (J cm^{-2})	Macro-crack width (μm)	Micro-crack width (μm)	Cellular sub-grain size (μm)
W	50	3.61 ± 0.33		
	80	7.75 ± 1.30	0.70 ± 0.12	0.34 ± 0.09
Mo	50		0.20 ± 0.03	0.18 ± 0.04
	80		1.15 ± 0.22	0.33 ± 0.06

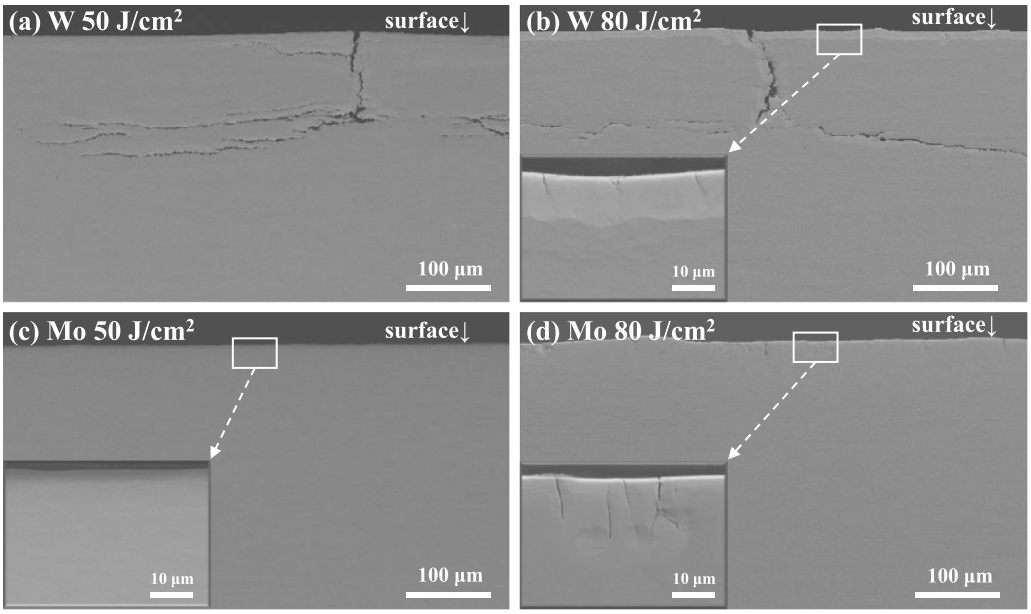

Figure 2. Cross-sectional SEM images of tungsten and molybdenum after irradiation at energy densities of 50 and 80 J cm^{-2}: (*a*) W 50 J cm^{-2}, (*b*) W 80 J cm^{-2}, (*c*) Mo 50 J cm^{-2}, (*d*) Mo 80 J cm^{-2}.

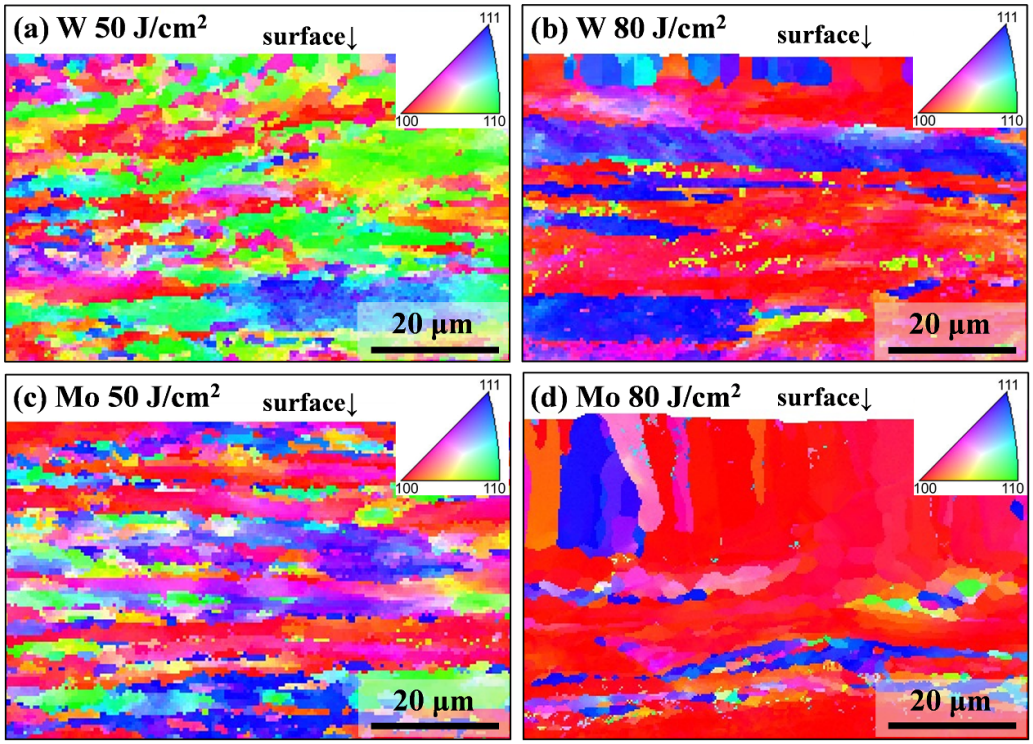

Figure 3. Cross-sectional EBSD images of tungsten and molybdenum after irradiation at energy densities of 50 and 80 J cm^{-2}: (*a*) W 50 J cm^{-2}, (*b*) W 80 J cm^{-2}, (*c*) Mo 50 J cm^{-2}, (*d*) Mo 80 J cm^{-2}.

For molybdenum irradiated at an energy density of 50 J cm^{-2} although micro-cracks appeared on the surface the depth was too small to be observed. The micro-crack depth of molybdenum was about 15 μm when the energy density increased to 80 J cm^{-2}.

Figure 3 shows the cross-sectional EBSD images of tungsten and molybdenum after irradiation at energy densities of 50 and 80 J cm^{-2}, and the cross-sectional grain maps and the grain orientation information in the direction normal to the surface can be seen. The region far away from the surface can be considered as the grain maps of unirradiated tungsten and molybdenum, which were composed of grains elongated parallel to the surface direction, and these were the typical grain maps of the rolled plates. No significant changes were

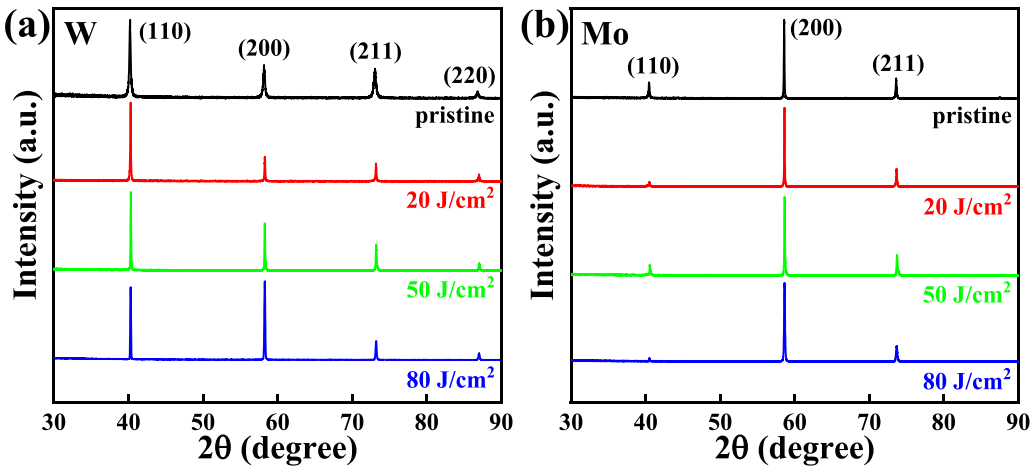

Figure 4. XRD patterns of (*a*) tungsten and (*b*) molybdenum before and after CPF irradiation.

observed in the grain maps of tungsten and molybdenum surfaces after irradiation at an energy density of 50 J cm^{-2}. When the energy density increased to 80 J cm^{-2}, columnar grains formed on the surfaces of both tungsten and molybdenum, and the thicknesses of the columnar grain layers were about 6 μm and 20 μm, respectively. For grain orientation, it can be seen from figures 3(*a*) and (*b*) that the grain orientation of tungsten was dominated by the <110> orientation after irradiation at 50 J cm^{-2} energy density, while at 80 J cm^{-2} energy density, the grain orientation became dominated by <100>. Molybdenum was dominated by the <100> orientation after both 50 and 80 J cm^{-2} irradiation. Moreover, in figures 3(*b*) and (*d*), the irradiation-induced columnar grains seemed to be dominated by the <100> orientation, especially in molybdenum. For further verification, the orientation changes were measured using XRD to exclude occasional cases due to the limited number of columnar grains measured by EBSD. Figure 4 shows the XRD patterns of tungsten and molybdenum before and after CPF irradiation. After irradiation at 20 and 50 J cm^{-2}, the (110) peak intensity of tungsten was the highest, which was the same as for pristine tungsten. When the energy density increased to 80 J cm^{-2}, the highest peak shifted to (200). For molybdenum, the intensity of the (200) peak was highest both before and after irradiation. The transmission rate of x-rays in the material can be expressed as

$$\frac{I}{I_0} = \mathrm{e}^{-\frac{\mu_\mathrm{m}\rho d}{\sin\theta}}, \tag{1}$$

where μ_m is the mass absorption coefficient, ρ is the density, d is the depth and θ is the incident angle. The mass absorption coefficient of Cu Kα x-rays in molybdenum is 164 cm^2 g^{-1}, and the intensity of the x-rays decays to less than 1% after penetrating to a depth of 20 μm, according to equation (1). Combined with the columnar grain layer thickness in figure 3, it can be assumed that the XRD results for molybdenum were mainly due to the diffraction of columnar grains when the energy density was 80 J cm^{-2}. In summary, columnar grains dominated by the <200> orientation (in the same direction as <100>) were created in tungsten and molybdenum after 80 J cm^{-2} irradiation.

Figure 5 shows the nano-hardness and its rate of change with depth for tungsten and molybdenum before and after CPF irradiation. For tungsten, the effect of irradiation at an energy density of 20 J cm^{-2} on hardness was not obvious; after 50 J cm^{-2} irradiation, softening occurred in the depth range within 2 μm; when the energy density increased to 80 J cm^{-2}, tungsten hardened where the depth was less than 0.7 μm while it softened in the region deeper than 0.7 μm. The molybdenum irradiated at 20 J cm^{-2} softened in the superficial area and then gradually approached the pristine state as the depth increased. After irradiation at energy densities of 50 and 80 J cm^{-2}, molybdenum hardened and then softened with increasing depth, with demarcation depths of about 0.3 μm and 0.7 μm for the hardened and softened regions, respectively. Compared with molybdenum, tungsten showed a smaller rate of change for hardness.

4. Thermal–mechanical simulation and discussion

Due to its strong heat and high power density, CPF irradiation is capable of depositing a large amount of energy on a material surface in a short period of time, and such transient thermal shock can cause serious damage to the material. After irradiation, melting waves, columnar grains, cellular sub-grain structure and cracks were observed on both tungsten and molybdenum surfaces. Macro-cracks and micro-cracks were present in tungsten, while only micro-cracks were present in molybdenum. The nano-hardness of the tungsten and molybdenum surfaces was also affected by CPF irradiation.

4.1. Thermal simulation of CPF irradiation

The evolution of the temperature of tungsten and molybdenum with time and space during CPF irradiation was analyzed by

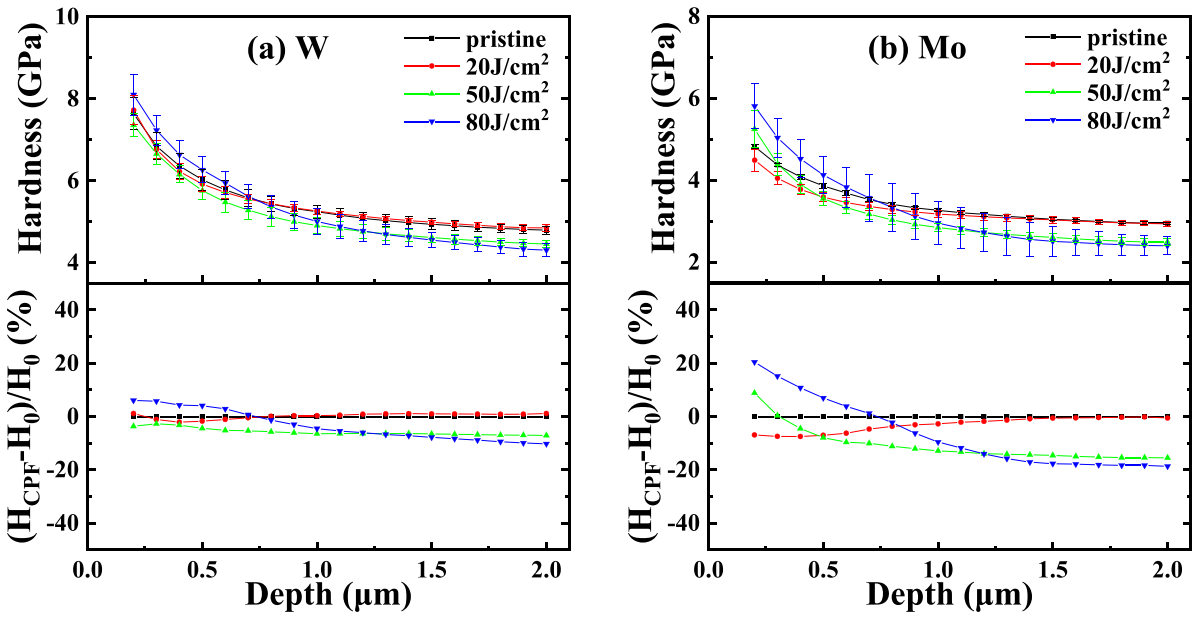

Figure 5. The nano-hardness and its rate of change with depth for (*a*) tungsten and (*b*) molybdenum before and after CPF irradiation.

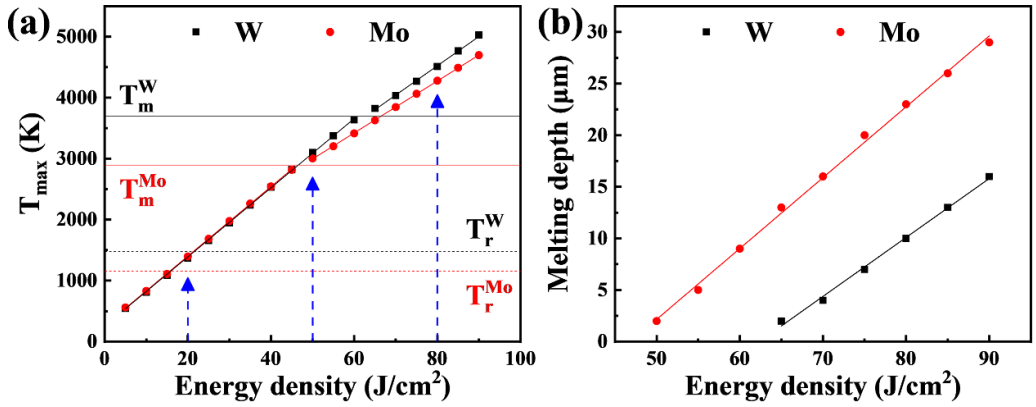

Figure 6. (*a*) The maximum temperature and (*b*) melting depth of tungsten and molybdenum with energy density.

the finite element method. The maximum temperatures (T_{max}) and melting depths (D_m) that can be reached for tungsten and molybdenum during the entire CPF irradiation process at different energy densities were calculated as shown in figure 6. Both T_{max} and D_m increased with increasing energy density. The T_{max} of tungsten and molybdenum can reach their T_m at energy densities of ∼61 J cm^{-2} and ∼46 J cm^{-2}, respectively. Under irradiation of 20, 50 and 80 J cm^{-2}, the temperature ranges of T_{max} in tungsten and molybdenum are indicated by the blue arrows in figure 6(*a*): at 20 J cm^{-2}, the T_{max} of tungsten was less than its T_r, while the T_{max} of molybdenum was between T_r and T_m; at 50 J cm^{-2}, the T_{max} of tungsten was between T_r and T_m, while the T_{max} of molybdenum was slightly larger than T_m; at 80 J cm^{-2}, the T_{max} of both tungsten and molybdenum was larger than their T_m.

Due to the drastic changes in physical properties before and after melting, the variation of T_{max} with energy density was approximately bilinear, with T_m as the demarcation temperature. The melting depth varied approximately linearly with energy density. The results of the linear fitting are shown in table 3. Interestingly, the T_{max} of tungsten and molybdenum were almost equal at energy densities of 45 J cm^{-2} and below, while the T_{max} of tungsten was significantly larger than that of molybdenum when the energy density was above 50 J cm^{-2}.

Table 3. Fitting results for maximum temperature and melting depth of tungsten and molybdenum as a function of energy density.

Material	ε (J cm^{-2})	T_{max} (K)	D_m (μm)
W	5–60	$243 + 57\varepsilon$	$-35.6 + 0.6\varepsilon$
	65–90	$658 + 48\varepsilon$	
Mo	5–45	$266 + 57\varepsilon$	$-32.2 + 0.7\varepsilon$
	50–90	$860 + 43\varepsilon$	

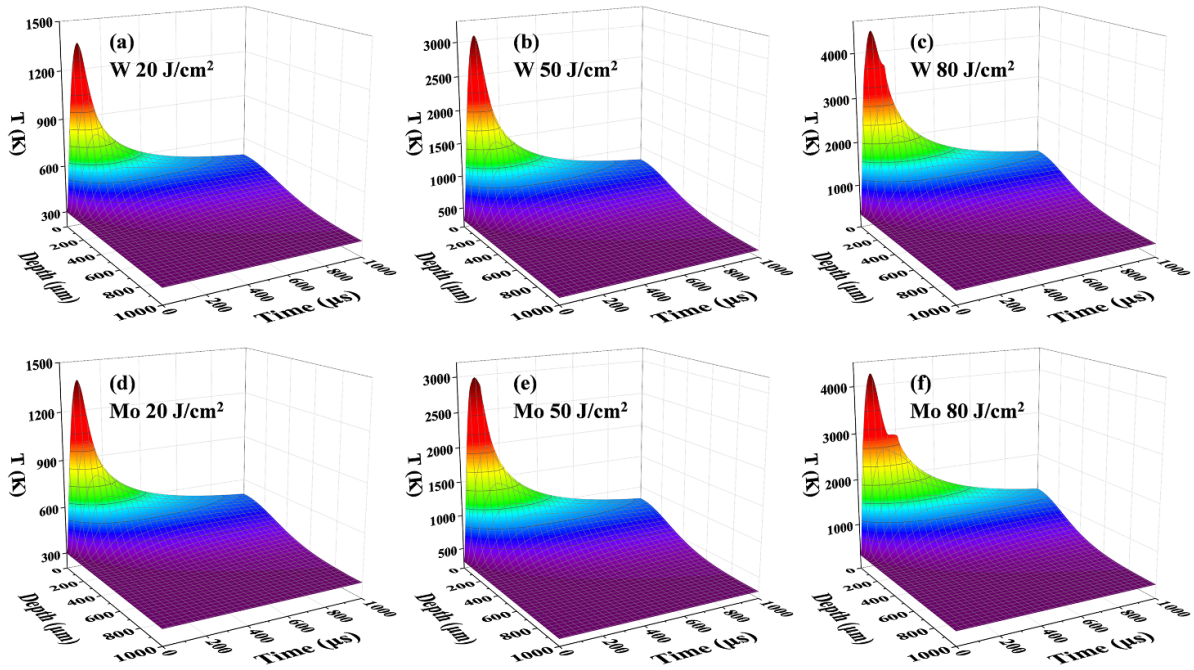

Figure 7. Evolution of temperature with time and space during CPF irradiation: (*a*) W 20 J cm^{-2}, (*b*) W 50 J cm^{-2}, (*c*) W 80 J cm^{-2}, (*d*) Mo 20 J cm^{-2}, (*e*) Mo 50 J cm^{-2}, (*f*) Mo 80 J cm^{-2}.

Since the heat flow distributed uniformly on surface, $T(z,t)$ can be described by the following non-stationary heat transfer equation [41] when considering only the temperature evolution in the depth (z) direction:

$$\rho(T)\,C(T)\,\frac{\partial T(z,t)}{\partial t}-\lambda(T)\,\frac{\partial^2 T(z,t)}{\partial z^2}=P(z,t)-\frac{\partial E_{\mathrm{ph}}}{\partial t}, \quad (2)$$

$$P(z,t)=\varepsilon\cdot d(z)\cdot f(t), \quad (3)$$

$$E_{\mathrm{ph}}=L\rho(T)\,h(T-T_{\mathrm{m}}), \quad (4)$$

$$h(T)=\begin{cases}1, T=0\\ 0, T\neq 0\end{cases} \quad (5)$$

where $\rho(T)$, $C(T)$, $\lambda(T)$ and L have been described in section 2. ε is the energy density and $P(z,t)$ is the heat source term, which was equal under the same energy density. $d(z)$ and $f(t)$ are both normalized functions, corresponding to the distribution functions of the heat flow with depth and time, respectively. E_{ph} is the term related to the latent heat of fusion. For tungsten and molybdenum, when the energy density was 45 J cm^{-2} and below, the $T_{\max}$ of both metals was less than T_{m}, thus the effect of latent heat of fusion could be neglected. According to equation (2), the temperature difference between tungsten and molybdenum derived from the difference in their density, specific heat and thermal conductivity. Due to the very short duration of heat flow under transient thermal shock irradiation, the effect of heat conduction on the heating efficiency was relatively small, meaning that the efficiency depended mainly on the product of density and specific heat. According to table 1, the products of density and specific heat of tungsten and molybdenum are almost equal, so they were similar in heating efficiency as well as $T_{\max}$ for irradiation at the same energy density. When the energy density was above 50 J cm^{-2}, $T_{\max}$ of molybdenum was less than that of tungsten. The reason is that molybdenum, with a lower T_{m}, melted before tungsten, and the subsequent solid–liquid transition process absorbed a large amount of heat, which reduced heating efficiency.

Figure 7 shows the evolution of temperature with time and space for CPF irradiation at energy densities of 20, 50 and 80 J cm^{-2}. A large amount of energy was deposited on the material surface within one pulse, causing a rapid increase in surface temperature with a maximum heating rate of about 10^7–10^8 K s^{-1}; subsequently, heat was transferred to the interior of the material and the surface temperature decreased quickly with a maximum cooling rate of about 10^7 K s^{-1}. With the increase of depth, the temperature decreased monotonically, and the maximum temperature gradient was up to the order of 10^8 K m^{-1}. Table 4 summarizes the calculated maximum temperature, melting depth, maximum heating/cooling rate and maximum temperature gradient for tungsten and molybdenum irradiated at three energy densities. The melting depth of tungsten irradiated at 80 J cm^{-2} was up to 10 μm, and the melting depth of molybdenum irradiated at 50 and 80 J cm^{-2} was about 2 and 23 μm, respectively. Due to the exotherm of solidification, the temperature of tungsten and molybdenum showed a cooling retardation zone near T_{m}, and this zone became more apparent when the melting depth was larger, as shown in figures 7(*c*), (*e*) and (*f*).

Table 4. Calculated results for the temperature fields of tungsten and molybdenum during CPF irradiation.

Material	ε (J cm^{-2})	T_{max} (K)	D_m (μm)	Maximum heating rate, 10^6 (K s^{-1})	Maximum cooling rate, 10^6 (K s^{-1})	Maximum temperature gradient, 10^6 (K m^{-1})
W	20	1369		22.1	7.3	20.8
	50	3100		58.9	18.4	63.6
	80	4512	10	96.8	48.8	130.1
Mo	20	1396		22.6	7.4	22.3
	50	3003	2	59.3	26.6	68.3
	80	4279	23	96.8	24.6	121.4

4.2. Melting waves, columnar grains and cellular sub-grains

A melting wave is a special surface characteristic induced by the rapid solidification of the molten layer when the mass migration is driven by a force parallel to the surface direction. There were two driving forces for surficial mass migration under CPF irradiation [13]: on the one hand, the molten surface was affected by gravity due to fact that the tungsten and molybdenum were perpendicular to the ground; on the other hand, the molten surface was also affected by the plasma pressure difference because the actual plasma distribution was not completely uniform on the surface.

It is generally believed that columnar grains are the common grain organization after directional solidification treatment, formed by heterogeneous nucleation and epitaxial growth. According to the results of temperature field calculation, the temperature distribution in the parallel surface direction was approximately uniform, and its temperature gradient was much smaller than that in the vertical surface direction ($\sim 10^8$ K m^{-1}) during CPF irradiation. The rapid directional solidification from the bottom of the molten layer toward the material surface induced the formation of columnar grains. Under the competitive growth mechanism, columnar grains tended to grow along the maximum heat extraction direction (i.e. the steepest temperature gradient) [42]. For crystals of cubic structure, columnar grains prefer to grow in the <100> orientation (in the same direction as <200>) [43]. As a result, a columnar grain structure dominated by the <200> orientation was generated after irradiation. The thickness of the columnar grain layer in tungsten and molybdenum irradiated with a CPF of 80 J cm^{-2} was about 6 μm and 20 μm, respectively, smaller than the calculated melting depths (10 μm and 23 μm), probably due to errors in the calculations, such as errors between the actual material properties and those entered in the simulations. For molybdenum irradiated at 50 J cm^{-2}, no obvious columnar grains were observed, which could be due to the melting depth being too small to form columnar grains.

According to the temperature field calculations, the temperature gradient within the molten layer reached as high as $\sim 10^8$ K m^{-1} during CPF irradiation, generated a huge surface tension gradient that drove the inevitable occurrence of strong thermocapillary convection (also known as Marangoni convection) and flow instability. Based on the theoretical model of thermocapillary convection, when convection and instability of the molten layer occurred only in the vertical direction, the flow pattern took the hexagonal cellular form under the action of the so-called Bénard–Marangoni instability [44–46]. In the case of simultaneous instability in the vertical and parallel directions, the competing results of the two determined the flow pattern: when the vertical direction dominated, the flow pattern showed a cellular structure; when the parallel direction dominated, the flow pattern exhibited a coiled/striped structure [47, 48]. For CPF irradiation, the temperature gradient in the direction of the parallel surface was too small to reach the instability condition, while the temperature gradient in the direction of the vertical surface was as high as $\sim 10^8$ K m^{-1}, leading to significant instability. As a result, convection with a hexagonal structure probably generated in the instable molten layer by the Bénard–Marangoni instability, and was superimposed on the solidified grain surfaces of tungsten and molybdenum, forming a unique cellular sub-grain structure. Moreover, due to the variations of the fluid flow condition and the molten layer oscillation, the ideal hexagonal structures usually lost geometric stability and eventually transformed to a cellular sub-grain structure with a mixture of hexagonal, pentagonal and quadrilateral shapes on the surface of tungsten and molybdenum after CPF irradiation [49]. In fact, this cellular sub-grain structure is also very common in high-energy beam material processing and rapid solidification, for example selective laser melting [48, 50, 51], welding [52] and directional solidification [53]. These technologies have similar characteristics in limiting grain growth.

4.3. Mechanical simulation and cracking behavior

Based on temperature field simulations, the stress and strain fields of tungsten and molybdenum during CPF irradiation were investigated by the finite element method with the aim of better understanding the emergence and extension of cracks. Tungsten and molybdenum at an irradiation energy density of 50 J cm^{-2} were chosen for the cracking study in the finite element simulation in order to exclude the influence of columnar grains on the calculation results.

Analysis of the transverse stress S_{xx} and transverse plastic strain PE_{xx} is necessary to understand the formation of longitudinal cracks. Figure 8 shows the time evolution of surface temperature, stress and plastic strain for tungsten and molybdenum at 50 J cm^{-2} irradiation. According to the evolution curve, the heating–cooling process can be divided into five stages [22, 23]. ① Compressive stress rising stage, where the

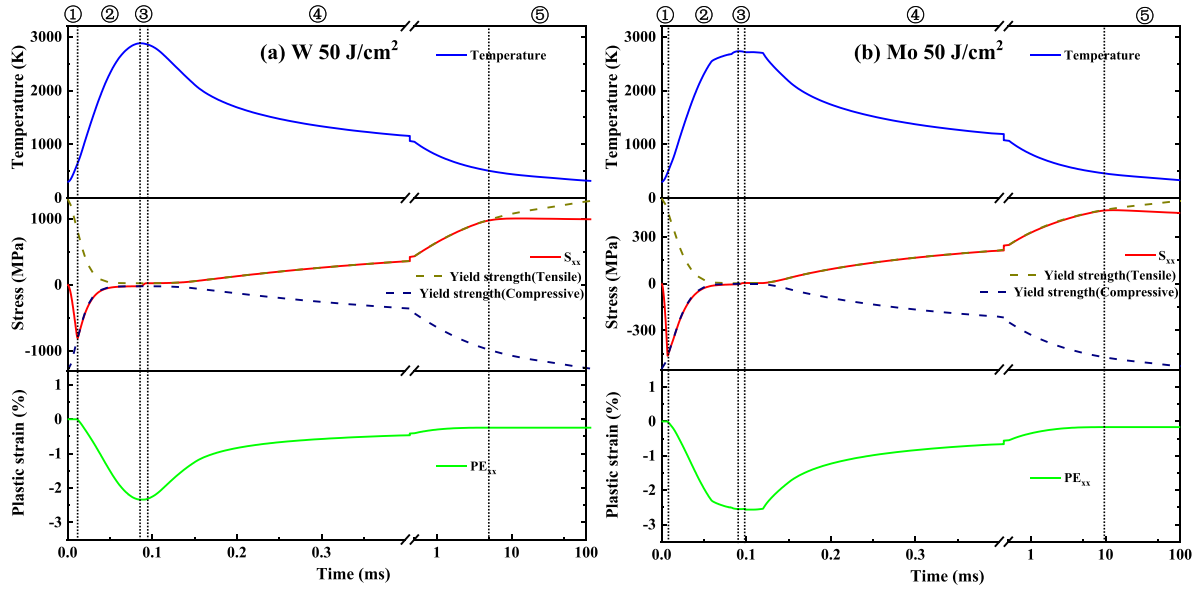

Figure 8. The time evolution of surface temperature, stress and plastic strain for (*a*) tungsten and (*b*) molybdenum at 50 J cm^{-2} irradiation.

surface temperature of tungsten and molybdenum increased rapidly under the heating of a transient thermal load, and the surface thermal expansion was constrained by the *x*/*y* direction, resulting in compressive stress. As the temperature increased, the stress value increased but the yield strength decreased until the two curves intersected, i.e. the material began to yield. In this stage, the stress was elastic and the plastic strain was zero. ② Compressive stress yielding stage, where the temperature increased until $T_{\max}$ and the absolute value of stress and yield strength decreased simultaneously. As tungsten and molybdenum yielded, plastic strain was generated and reached a peak at $T_{\max}$. ③ Compressive–tensile stress transition stage, where the transient heat flow vanished. The surface temperature started to decrease rapidly due to heat transfer to the interior of the material, and S_{xx} changed from compressive stress to tensile stress. The yield strength increased with decreasing temperature. At this stage, the absolute value of the stress was lower than the yield strength, so yielding paused and the plastic strain remained constant. ④ Tensile stress yielding stage, where the rapid decrease of temperature caused the tensile stress to reach the yield strength again, the material underwent plastic deformation opposite to the second stage, and the plastic strain gradually recovered. ⑤ Tensile stress yielding stop stage, where the cooling rate gradually decreased with time, the tensile stress was less than the yield strength after reaching the critical point, and the tensile stress yielding stopped. Eventually, the tensile stress remained on the surfaces of the CPF-irradiated tungsten and molybdenum, and the plastic strain on the surfaces could not be fully restored to the unirradiated state.

It is well known that when the temperature is higher than the DBTT, the material shows ductile characteristics and plastic deformation does not cause cracking, while when the temperature is lower than the DBTT, the material changes from

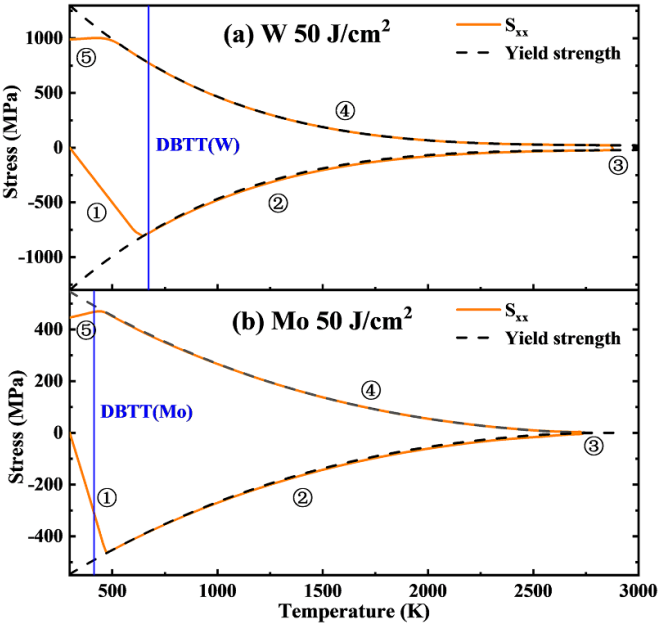

Figure 9. Stress–temperature curves of (*a*) tungsten and (*b*) molybdenum surfaces at 50 J cm^{-2} irradiation.

ductile to brittle, and even a small plastic deformation will induce cracking [37]. Therefore, the cracking condition for tungsten and molybdenum during CPF irradiation is that the tensile stress value reaches the yield strength when the temperature is below the DBTT [23]. Based on this, figure 9 shows the relationship between stress and temperature, where ①–⑤ correspond to the five stages of figure 8. It can be noted that during the cooling process (stages ③–⑤), tungsten was still in the tensile stress yielding stage while molybdenum entered the tensile stress yield stopping stage when the surface temperature dropped below the DBTT. Therefore, brittleness-induced

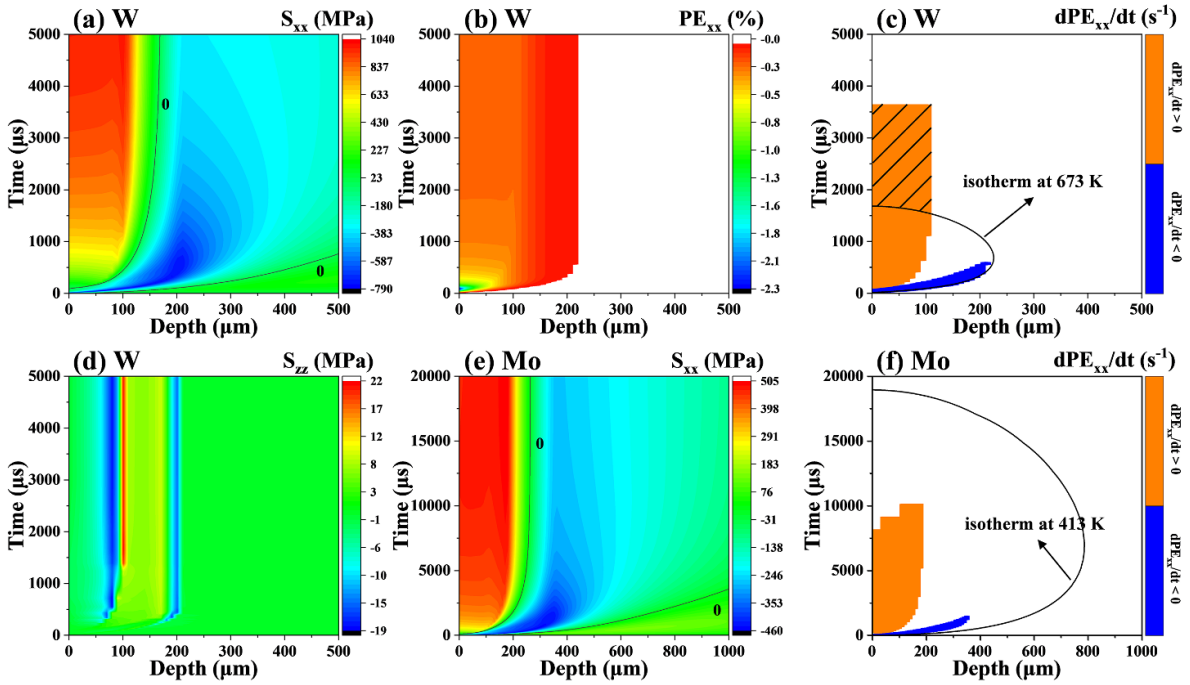

Figure 10. Evolution of (*a*) S_{xx}, (*b*) PE_{xx}, (*c*) dPE_{xx}/dt, (*d*) S_{zz} for tungsten and (*e*) S_{xx}, (*f*) dPE_{xx}/dt for molybdenum with time and space at 50 J cm^{-2} irradiation.

macro-cracks were generated on the tungsten surface, while no macro-cracks were observed on the molybdenum surface, in agreement with the SEM results in figure 1. For micro-cracks, the melting and re-solidification in ELM-like thermal shock irradiation experiments led to embrittlement [3], so the DBTT in the re-solidified zone was larger than the DBTT of the matrix labeled in figure 9. Combined with the stress–temperature curve of molybdenum, the re-solidification zone was likely to remain in the tensile stress yielding stage when the surface temperature dropped below the DBTT of the re-solidification zone, implying the formation of micro-cracks. The width of the micro-cracks increased with increasing melting depth.

Figure 10 shows the relationship of stress and strain with depth during CPF irradiation, which is intended to analyze the evolution of cracks extending in the depth direction. Figure 10(*a*) is the variation of the transverse stress of tungsten with time and depth at 50 J cm^{-2} irradiation, where positive and negative values represent tensile and compressive stress, respectively. The evolution map of transverse stress can be divided into compressive and tensile stress zones: in the initial stage of irradiation, there was only compressive stress in the tungsten, and after heat flow stopped the surface temperature decreased due to directional heat extraction, leading to the generation of tensile stress. The dividing line between the two zones is at a depth of about 150 μm. When the stress exceeded the yield strength, plastic strain occurred, with its influence to a depth of about 230 μm (figure 10(*b*)). The strain rate can reflect whether the material was in the yield stage (i.e. whether the stress reached the yield strength), as shown in figure 10(*c*). The orange zone is the tensile stress yield zone, the blue zone is the compressive stress yield zone and the black curve is the DBTT isotherm of tungsten. The range of influence of the tensile stress yield zone was at a depth of about 0–110 μm, while that of the compressive stress yield zone extended to a depth of about 230 μm. According to the criterion of crack formation, cracks formed in the tensile stress yield zone with temperatures below the DBTT, which is shaded in figure 10(*c*). As can be seen from the figure, the cracks can easily extend longitudinally to a depth of about 110 μm. It is noteworthy that longitudinal tensile stresses were also generated in tungsten at a depth of about 110 μm during irradiation (red line in figure 10(*d*)). Since the finite element model did not consider the local deformation generated by the formation of longitudinal cracks, the actual longitudinal tensile stress value was larger than the calculated value [27]. The transverse transformation of longitudinal cracks could be induced by longitudinal tensile stress and other factors, such as the direction of long grains parallel to the surface of the rolled sheet, and the inertia of motion during the formation of longitudinal cracks [27]. In addition, in the shaded zone of crack formation in figure 10(*c*), it can be noticed that the time when cracks started to form on the tungsten surface was later than those at about 110 μm depth, which meant that the cracks may preferentially sprout inside the material [35, 54]. Figures 10(*e*) and (*f*) show the evolution of transverse stress and transverse plastic strain rate of molybdenum at 50 J cm^{-2} irradiation, respectively. The tensile yield zone and the compressive yield zone can reach larger depths of about 190 μm and 370 μm, respectively, because the yield strength of molybdenum is smaller than that of tungsten. However, the DBTT of molybdenum is much smaller than that of tungsten, and there is no overlap between the zone below the DBTT and the tensile

Table 5. Correspondence between the hardness change and the temperature range of T_{max}.

Material	ε (J cm^{-2})	Hardness change with depth	Demarcation depth of hardening and softening (μm)	Temperature range
W	20	Almost unchanged		$T_{max} < T_r$
	50	Softening		$T_r < T_{max} < T_m$
	80	Hardening first, then softening	0.7	$T_{max} > T_m$
Mo	20	Softening first, then unchanged		$T_r < T_{max} < T_m$
	50	Hardening first, then softening	0.3	$T_{max} > T_m$
	80	Hardening first, then softening	0.7	$T_{max} > T_m$

yield zone, making it difficult for macro-cracks to sprout in molybdenum.

4.4. Hardening and softening

Table 5 shows the correspondence between the hardness change and the temperature range of T_{max} for tungsten and molybdenum. As can be seen, when $T_{max} < T_r$, the effect of irradiation on hardness is not obvious; when $T_r < T_{max} < T_m$, tungsten and molybdenum softened; when $T_{max} > T_m$, tungsten and molybdenum hardened first and then softened with increasing depth. On the one hand, hardening occurred only in the case of $T_{max} > T_m$, indicating that hardening was related to the re-solidification process; on the other hand, the demarcation depth between hardening and softening was much smaller than the thickness of the columnar grain layer, which implied that columnar grains softened the material. Studies by Thijs *et al* [55] and Qian *et al* [56] both pointed out that the small-sized cellular sub-grains produced by re-solidification increased the surface hardness of the material, which was also probably responsible for the surface hardening of tungsten and molybdenum after CPF irradiation. Softening occurred as soon as $T_{max} > T_r$. The thermal effect on the recovery of the microstructure [54] and the formation of columnar grains both probably reduced the hardness. It can be seen that the change in hardness after irradiation is the result of competition between several factors.

5. Conclusions

The irradiation damage mechanisms of tungsten and molybdenum under ELM-like thermal shock was discussed by combining CPF irradiation experiments with finite element simulations. The following conclusions were obtained:

(1) When the CPF irradiation was sufficient to melt the tungsten and molybdenum, a melting wave was formed by the rapid solidification of the molten layer when mass migration was driven by the force parallel to the surface direction. The rapid directional solidification of the melt from the bottom of the molten layer toward the material surface induced the formation of columnar grains dominated by the <200> orientation. The high temperature gradient during rapid solidification caused significant instability in the molten layer and generated strong thermocapillary convection. A structure of submicron-sized cellular subgrains formed on the material surface under the action of Bénard–Marangoni instability.

(2) After CPF irradiation, macro-cracks and micro-cracks were produced on the surface of tungsten, while only micro-cracks were found in molybdenum. The macro-cracks occurred due to the intrinsic brittleness of tungsten (high DBTT) and the micro-cracks were created by the embrittlement of the re-solidification layer. From the finite element simulation, the crack formation zone (the region where the temperature was less than the DBTT and the transverse tensile stress reached the yield strength) of tungsten ranged from the surface to the interior with a depth of 110 μm, and longitudinal tensile stress was generated at the boundary of the crack formation zone. The macro-cracks in tungsten first extended longitudinally from the surface to the interior and then the direction of extension changed from longitudinal to transverse as a result of stress evolution.

(3) The change in hardness of tungsten and molybdenum after CPF irradiation was the result of competition between several factors: on the one hand, the thermal effect on the recovery of the microstructure and the formation of columnar grains decreased the hardness; on the other hand, the formation of a submicron-sized cellular subgrain structure increased the hardness. When $T_{max} < T_r$, the effect of irradiation on hardness was not obvious; when $T_r < T_{max} < T_m$, tungsten and molybdenum both softened; when $T_{max} > T_m$, tungsten and molybdenum hardened first and then softened with increasing depth. Compared with molybdenum, tungsten showed a smaller rate of change of hardness.

Acknowledgments

This work was supported by the National Natural Science Foundation of China (Nos. 11975065 and 12211530445).

Appendix. Supplementary information related to the finite element model

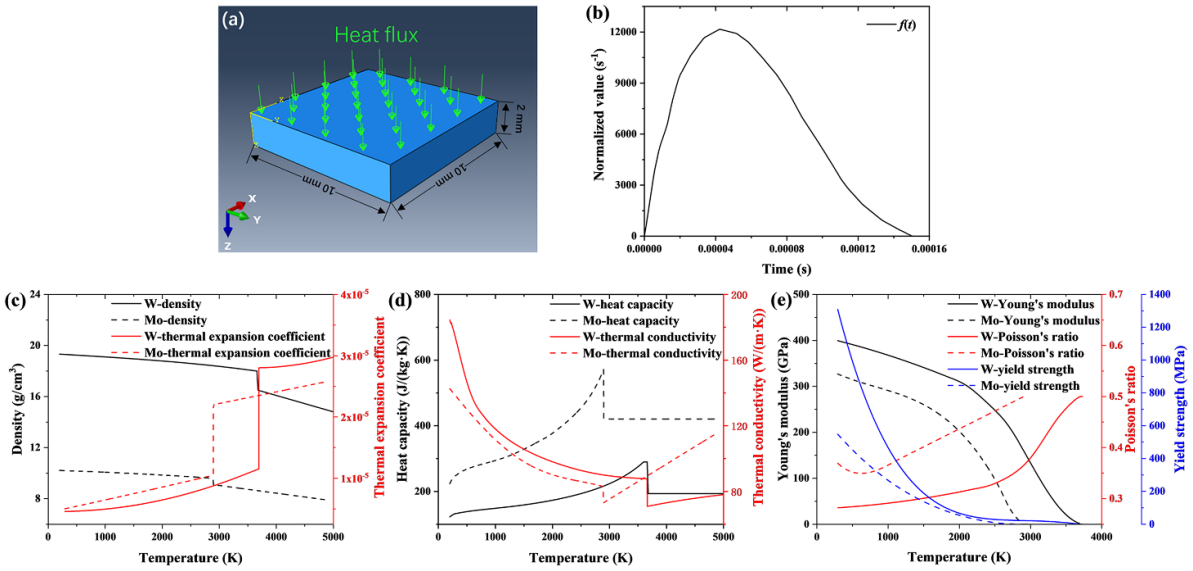

Figure A1. (*a*) Three-dimensional finite element model. (*b*) The distribution of heat flow with time. (*c*)–(*e*) The physical properties of tungsten and molybdenum with temperature.

References

[1] Herrmann A., Eich T., Jachmich S., Laux M., Andrew P., Bergmann A., Loarte A., Matthews G. and Neuhauser J. 2003 Stationary and transient divertor heat flux profiles and extrapolation to ITER *J. Nucl. Mater.* **313–316** 759–67

[2] Ueda Y., Coenen J.W., De Temmerman G., Doerner R.P., Linke J., Philipps V. and Tsitrone E. 2014 Research status and issues of tungsten plasma facing materials for ITER and beyond *Fusion Eng. Des.* **89** 901–6

[3] Budaev V.P. 2016 Results of high heat flux tests of tungsten divertor targets under plasma heat loads expected in ITER and tokamaks (review) *Phys. At. Nucl.* **79** 1137–62

[4] Kaufmann M. and Neu R. 2007 Tungsten as first wall material in fusion devices *Fusion Eng. Des.* **82** 521–7

[5] Taylor N.P. and Pampin R. 2006 Activation properties of tungsten as a first wall protection in fusion power plants *Fusion Eng. Des.* **81** 1333–8

[6] Litnovsky A., Voitsenya V.S., Costley A. and Donné A.J.H. 2007 First mirrors for diagnostic systems of ITER *Nucl. Fusion* **47** 833–8

[7] Wisse M., Eren B., Marot L., Steiner R. and Meyer E. 2012 Spectroscopic reflectometry of mirror surfaces during plasma exposure *Rev. Sci. Instrum.* **83** 013509

[8] Peng J., Chen L.W., Yan R., Chen J.L., Zhu D.H., Ding R., Wang Q. and Zhang Z.M. 2016 Comparative investigations of stainless steel and molybdenum first mirrors cleaning using radio frequency plasma *Fusion Eng. Des.* **112** 317–23

[9] Budaev V.P. *et al* 2015 Tungsten recrystallization and cracking under ITER-relevant heat loads *J. Nucl. Mater.* **463** 237–40

[10] Arzhannikov A.V. *et al* 2013 Surface modification and droplet formation of tungsten under hot plasma irradiation at the GOL-3 *J. Nucl. Mater.* **438** S677–80

[11] Yu J.H., Simmonds M.J., Baldwin M.J. and Doerner R.P. 2019 Deuterium retention in re-solidified tungsten and beryllium *Nucl. Mater. Energy* **18** 297–306

[12] Shymanski V.I., Uglov V.V., Cherenda N.N., Pigasova V.S., Astashynski V.M., Kuzmitski A.M., Zhong H.W., Zhang S.J., Le X.Y. and Remnev G.E. 2019 Structure and phase composition of tungsten alloys modified by compression plasma flows and high-intense pulsed ion beam impacts *Appl. Surf. Sci* **491** 43–52

[13] Qu M., Kong F., Yan S., Uglov V.V., Xue J. and Wang Y. 2019 Damages on pure tungsten irradiated by compression plasma flows *Nucl. Instrum. Methods Phys. Res.* B **444** 33–37

[14] Makhlay V.A., Bandura A.N., Byrka O.V., Garkusha I.E., Chebotarev V.V., Tereshin V.I. and Landman I. 2007 Effect of preheating on the damage to tungsten targets after repetitive ITER ELM-like heat loads *Phys. Scr.* T **T128** 239–41

[15] Makhlaj V.A., Garkusha I.E., Aksenov N.N., Chuvilo A.A., Chebotarev V.V., Landman I., Malykhin S.V., Pestchanyi S. and Pugachov A.T. 2013 Dust generation mechanisms under powerful plasma impacts to the tungsten surfaces in ITER ELM simulation experiments *J. Nucl. Mater.* **438** S233–6

[16] Yakushin V., Polsky V., Kalin B., Dzhumaev P., Polyansky A., Sevryukov O., Suchkov A. and Fedotov V. 2013 Erosion of tungsten and its brazed joints with bronze irradiated by pulsed deuterium plasma flows *J. Nucl. Mater.* **442** S237–41

[17] Shoshin A.A. *et al* 2011 Plasma-surface interaction during ITER type I ELMs: comparison of simulation with QSPA Kh-50 and the GOL-3 facilities *Fusion Sci. Technol.* **59** 57–60

[18] Ankudinov A.V., Voronin A.V., Gusev V.K., Gerasimenko Y.A., Demina E.V., Prusakova M.D. and Sud'enkov Y.V. 2014 Influence of a plasma jet on different types of tungsten *Tech. Phys.* **59** 346–52

[19] Makhlaj V.A. *et al* 2014 Plasma exposure of different tungsten grades with plasma accelerators under ITER-relevant conditions *Phys. Scr.* **T161** 014040

[20] Li X., Zhu D., Li C. and Chen J. 2017 Cracking and grain refining behaviors of tungsten based plasma facing materials under fusion relevant transient heat flux *Fusion Eng. Des.* **125** 515–20

[21] Garkusha I.E., Landman I., Linke J., Makhlaj V.A., Medvedev A.V., Malykhin S.V., Peschanyi S., Pintsuk G., Pugachev A.T. and Tereshin V.I. 2011 Performance of

deformed tungsten under ELM-like plasma exposures in QSPA Kh-50 *J. Nucl. Mater.* **415** S65–9
[22] Arakcheev A.S. *et al* 2015 A theoretical investigation of crack formation in tungsten after heat loads *J. Nucl. Mater.* **463** 246–9
[23] Li C., Zhu D., Li X., Wang B. and Chen J. 2017 Thermal–stress analysis on the crack formation of tungsten during fusion relevant transient heat loads *Nucl. Mater. Energy* **13** 68–73
[24] Li C., Zhu D., Wang B. and Chen J. 2018 Theoretical analysis on the damages for tungsten plasma facing surface under superposition of steady-state and transient heat loads *Fusion Eng. Des.* **132** 99–106
[25] Hirai T., Pintsuk G., Linke J. and Batilliot M. 2009 Cracking failure study of ITER-reference tungsten grade under single pulse thermal shock loads at elevated temperatures *J. Nucl. Mater.* **390–391** 751–4
[26] Yuan Y., Du J., Wirtz M., Luo G.N., Lu G.H. and Liu W. 2016 Surface damage and structure evolution of recrystallized tungsten exposed to ELM-like transient loads *Nucl. Fusion* **56** 036021
[27] Arakcheev A.S. *et al* 2019 On the mechanism of surface-parallel cracks formation under pulsed heat loads *Nucl. Mater. Energy* **20** 100677
[28] Vasilyev A.A. *et al* 2017 *In-situ* imaging of tungsten surface modification under ITER-like transient heat loads *Nucl. Mater. Energy* **12** 553–8
[29] Garkusha I.E., Makhlai V.A., Aksenov N.N., Bazylev B., Landman I., Sadowski M. and Skladnik-Sadowska E. 2014 Tungsten melt losses under QSPA Kh-50 plasma exposures simulating ITER ELMS and disruptions *Fusion Sci. Technol.* **65** 186–93
[30] Wirtz M., Cempura G., Linke J., Pintsuk G. and Uytdenhouwen I. 2013 Thermal shock response of deformed and recrystallised tungsten *Fusion Eng. Des.* **88** 1768–72
[31] Farid N., Zhao D., Oderji H.Y. and Ding H. 2015 Cracking and damage behavior of tungsten under ELM's like energy loads using millisecond laser pulses *J. Nucl. Mater.* **463** 241–5
[32] Huber A. *et al* 2014 Investigation of the impact of transient heat loads applied by laser irradiation on ITER-grade tungsten *Phys. Scr.* **T159** 014005
[33] Wirtz M., Linke J., Pintsuk G., Singheiser L. and Zlobinski M. 2013 Comparison of thermal shock damages induced by different simulation methods on tungsten *J. Nucl. Mater.* **438** S833–6
[34] Huber A. *et al* 2013 Investigation of the impact on tungsten of transient heat loads induced by laser irradiation, electron beams and plasma guns *Fusion Sci. Technol.* **63** 197–200
[35] Li M., Werner E. and You J.H. 2015 Cracking behavior of tungsten armor under ELM-like thermal shock loads: a computational study *Nucl. Mater. Energy* **2** 1–11
[36] Du J., Yuan Y., Wirtz M., Linke J., Liu W. and Greuner H. 2015 FEM study of recrystallized tungsten under ELM-like heat loads *J. Nucl. Mater.* **463** 219–22
[37] Liu X., Lian Y., Chen L., Chen Z., Chen J., Duan X., Fan J. and Song J. 2015 Experimental and numerical simulations of ELM-like transient damage behaviors to different grade tungsten and tungsten alloys *J. Nucl. Mater.* **463** 166–9
[38] Zhu Q., Xie M., Shang X., An G., Sun J., Wang N., Xi S., Bu C. and Zhang J. 2020 Research status and progress of welding technologies for molybdenum and molybdenum alloys *Metals* **10** 279
[39] Cherenda N.N., Uglov V.V., Anishchik V.M., Stalmashonak A.K., Astashinski V.M., Kuzmickii A.M., Punko A.V., Thorwath G. and Stritzker B. 2006 Modification of high-speed steels by nitrogen compression plasma flow: structure, element composition, tribological properties *Surf. Coat. Technol.* **200** 5334–42
[40] Cherenda N.N., Basalai A.V., Uglov V.V., Laskovnev A.P., Astashynski V.M. and Kuzmitski A.M. 2019 Phase composition and mechanical properties of Cu–Ti alloys synthesized in the surface layer of copper by plasma impact on the Ti/Cu system *Vacuum* **167** 452–8
[41] Zhang J., Zhong H., Shen J., Yu X., Yan S. and Le X. 2020 The influence of metal surface topography on ablation behavior during intense pulsed ion beam irradiation *Surf. Coat. Technol.* **388** 125599
[42] Zhou X., Li K., Zhang D., Liu X., Ma J., Liu W. and Shen Z. 2015 Textures formed in a CoCrMo alloy by selective laser melting *J. Alloys Compd.* **631** 153–64
[43] Liu X., Zhao C., Zhou X., Shen Z. and Liu W. 2019 Microstructure of selective laser melted AlSi10Mg alloy *Mater. Des.* **168** 107677
[44] Schwabe D. 2007 Convective instabilities in complex systems with partly free surface *J. Phys. Conf. Ser.* **64** 012001
[45] Shklyaev O.E. and Nepomnyashchy A.A. 2004 Thermocapillary flows under an inclined temperature gradient *J. Fluid Mech.* **504** 99–132
[46] Shtilman L. and Sivashinsky G. 1991 Hexagonal structure of large-scale Marangoni convection *Phys.* D **52** 477–88
[47] Mizev A.I. and Schwabe D. 2009 Convective instabilities in liquid layers with free upper surface under the action of an inclined temperature gradient *Phys. Fluids* **21** 112102
[48] Liu X., Zhou X., Xu B., Ma J., Zhao C., Shen Z. and Liu W. 2019 Morphological development of sub-grain cellular/bands microstructures in selective laser melting *Materials* **12** 1204
[49] Schatz M.F., VanHook S.J., McCormick W.D., Swift J.B. and Swinney H.L. 1999 Time-independent square patterns in surface-tension-driven Bénard convection *Phys. Fluids* **11** 2577–82
[50] Yadroitsev I., Krakhmalev P., Yadroitsava I., Johansson S. and Smurov I. 2013 Energy input effect on morphology and microstructure of selective laser melting single track from metallic powder *J. Mater. Process. Technol.* **213** 606–13
[51] Ma M., Wang Z., Gao M. and Zeng X. 2015 Layer thickness dependence of performance in high-power selective laser melting of 1Cr18Ni9Ti stainless steel *J. Mater. Process. Technol.* **215** 142–50
[52] Phanikumar G., Dutta P. and Chattopadhyay K. 2005 Continuous welding of Cu–Ni dissimilar couple using CO_2 laser *Sci. Technol. Weld. Join* **10** 158–66
[53] Bergeon N., Mota F.L., Chen L., Tourret D., Debierre J.M., Guérin R., Karma A., Billia B. and Trivedi R. 2015 Dynamical microstructure formation in 3D directional solidification of transparent model alloys: *in situ* characterization in DECLIC directional solidification insert under diffusion transport in microgravity *IOP Conf. Ser.: Mater. Sci. Eng.* **84** 012077
[54] Bakaeva A., Makhlai V., Terentyev D., Zinovev A., Herashchenko S. and Dubinko A. 2019 Correlation of hardness and surface microcracking in ITER specification tungsten exposed at QSPA Kh-50 *J. Nucl. Mater.* **520** 185–92
[55] Thijs L., Kempen K., Kruth J.-P. and Van Humbeeck J. 2013 Fine-structured aluminium products with controllable texture by selective laser melting of pre-alloyed AlSi10Mg powder *Acta Mater.* **61** 1809–19
[56] Qian B., Saeidi K., Kvetková L., Lofaj F., Xiao C. and Shen Z. 2015 Defects-tolerant Co-Cr-Mo dental alloys prepared by selective laser melting *Dent. Mater.* **31** 1435–44